Catalyst screening for the Oxidative Coupling of Methane: from isothermal to adiabatic operation via microkinetic simulations

Supplementary Information

Laura Pirro[†], *Pedro S. F. Mendes*[†], *Bart D. Vandegehuchte*[‡], *Guy B. Marin*[†], *Joris W. Thybaut*[*,†]

† Laboratory for Chemical Technology, Ghent University, Technologiepark 125, B-9052 Ghent, Belgium

‡ Total Research & Technology Feluy, Zone Industrielle Feluy C B-7181, Seneffe, Belgium

Table of Contents

S1. Overview of the OCM microkinetic and reactor model

The OCM microkinetic model adopted in the present work accounts for the complex chemistry of the reaction via 78 gas-phase and 52 catalytic elementary steps[1]. The reaction network is herein reported in Tables S1.1 and S1.2. It includes 13 molecules (H_2, H_2O, H_2O_2, O_2, CH_4, CH_2O, CO, CO_2, C_2H_2, C_2H_4, C_2H_6, C_3H_6, C_3H_8), 10 radicals (H•, O•, OH•, HO_2•, CHO•, CH_3O•, CH_3•, C_2H_3•, C_2H_5•, C_3H_7•), 10 surface species (O*, OH*, H_2O*, CO*, CO_2*, CHO*, CH_2O*, CH_3O*, C_2H_3O*, C_2H_4O*) and the free active sites *. The incorporation of catalyst descriptors, such as chemisorption enthalpies, sticking probabilities and active site density, allows to establish a link between catalyst properties and their performance in the OCM reaction[2]. This model was validated using experimental data from five different catalysts (Li/MgO[3], Sn-Li/MgO[3], Sr/La_2O_3[4], La-Sr/CaO[4], Na-Mn-W/SiO_2[4, 5]) at a broad range of operating conditions.

The catalytic fixed-bed reactor model, in which the above mentioned microkinetic model is incorporated, consists of a 1-dimensional plug flow reactor, i.e. no radial concentration and temperature gradients were considered on the reactor scale. The reactor model allows simulation in both isothermal[1] and adiabatic mode[6]. Axial diffusion and thermal conduction on the reactor scale were considered negligible, as typical for tubular reactors of high aspect ratio[7]. Given the fact that the participating gas-phase intermediates are highly reactive and cause irreducible mass transport limitations on the particle scale, the model is heterogeneous. Two phases are considered[8]: the *intraparticle* phase consists of the catalyst particles and the gas contained in their pores; the *interstitial* phase accounts for the gas phase around the particles and flowing along the reactor axis. Particle-scale concentration gradients for gas-phase molecules and, more significantly, for radicals and surface species, are accounted for in the reactor model[1]. Only external heat transport limitations in the gas phase surrounding the

particles are considered, with no temperature gradients inside the catalyst particles in view of the high thermal conductivity of the catalytic materials[6].

50 *Table S1.1. Gas-phase reaction network; kinetic parameters are reported by Chen et al.[9].*

Primary initiation	**Dehydrogenation of C_2-C_3**
G1. $CH_4 + O_2 \rightleftharpoons CH_3\bullet + HO_2\bullet$	G19. $C_2H_6 + H\bullet \rightleftharpoons C_2H_5\bullet + H_2$
$CH_3\bullet$ generation	G20. $C_2H_6 + OH\bullet \rightleftharpoons C_2H_5\bullet + H_2O$
G2. $CH_4 + H\bullet \rightleftharpoons CH_3\bullet + H_2$	G21. $C_2H_6 + CH_3\bullet \rightleftharpoons C_2H_5\bullet + CH_4$
G3. $CH_4 + O\bullet \rightleftharpoons CH_3\bullet + OH\bullet$	G22. $C_2H_5\bullet + M \rightleftharpoons C_2H_4 + H\bullet + M$
G4. $CH_4 + OH\bullet \rightleftharpoons CH_3\bullet + H_2O$	G23. $C_2H_5\bullet + O_2 \rightleftharpoons C_2H_4 + HO_2\bullet$
G5. $CH_4 + HO_2\bullet \rightleftharpoons CH_3\bullet + H_2O_2$	G24. $C_2H_4 + O_2 \rightleftharpoons C_2H_3\bullet + HO_2\bullet$
$CH_3\bullet$ oxidation	G25. $C_2H_4 + H\bullet \rightleftharpoons C_2H_3\bullet + H_2$
G6. $CH_3\bullet + O_2 \rightleftharpoons CH_3O\bullet + O\bullet$	G26. $C_2H_4 + OH\bullet \rightleftharpoons C_2H_3\bullet + H_2O$
G7. $CH_3\bullet + O_2 \rightleftharpoons CH_2O + OH\bullet$	G27. $C_2H_4 + CH_3\bullet \rightleftharpoons C_2H_3\bullet + CH_4$
G8. $CH_3\bullet + HO_2\bullet \rightleftharpoons CH_3O\bullet + OH\bullet$	G28. $C_2H_3\bullet + M \rightleftharpoons C_2H_2 + H\bullet + M$
Coupling Reactions	G29. $C_2H_3\bullet + O_2 \rightleftharpoons C_2H_2 + HO_2\bullet$
G9. $CH_3\bullet + CH_3\bullet + M \rightleftharpoons C_2H_6 + M$	G30. $C_3H_8 + H\bullet \rightleftharpoons C_3H_7\bullet + H_2$
G10. $C_2H_5\bullet + CH_3\bullet + M \rightleftharpoons C_3H_8 + M$	G31. $C_3H_7\bullet + M \rightleftharpoons C_3H_6 + H\bullet + M$
G11. $C_2H_4 + CH_3\bullet + M \rightleftharpoons C_3H_7\bullet + M$	G32. $C_2H_6 \rightleftharpoons C_2H_5\bullet + H\bullet$
Oxidation of $CH_3O\bullet$ and CH_2O	**C_2 Oxidation**
G12. $CH_3O\bullet + M \rightleftharpoons CH_2O + H\bullet + M$	G33. $C_2H_5\bullet + HO_2\bullet \rightleftharpoons CH_3\bullet + CH_2O + OH\bullet$
G13. $CH_2O + OH\bullet \rightleftharpoons CHO\bullet + H_2O$	G34. $C_2H_4 + OH\bullet \rightleftharpoons CH_3\bullet + CH_2O$
G14. $CH_2O + HO_2\bullet \rightleftharpoons CHO\bullet + H_2O_2$	G35. $C_2H_3\bullet + O_2 \rightleftharpoons CH_2O + CHO\bullet$
G15. $CH_2O + CH_3\bullet \rightleftharpoons CHO\bullet + CH_4$	**Hydrogen–oxygen reactions**
G16. $CHO\bullet + M \rightleftharpoons CO + H\bullet + M$	G36. $O_2 + H\bullet \rightleftharpoons OH\bullet + O\bullet$
G17. $CHO\bullet + O_2 \rightleftharpoons CO + HO_2\bullet$	G37. $O_2 + H\bullet + M \rightleftharpoons HO_2\bullet + M$
G18. $CO + HO_2\bullet \rightleftharpoons CO_2 + OH\bullet$	G38. $HO_2\bullet + HO_2\bullet \rightleftharpoons O_2 + H_2O_2$
	G39. $H_2O_2 + M \rightleftharpoons OH\bullet + OH\bullet + M$

51 M is any molecule which acts as third body, stabilizing the collision product.

Table S1.2. Catalytic reaction network; Surface reactions[1] grouped by their function.

Oxygen activation	C13. $CHO^* + O^* \rightleftharpoons CO^* + OH^*$
C1. $O_2 + 2^* \rightleftharpoons 2O^*$	C14. $CO^* + O^* \rightleftharpoons CO_2^* + ^*$
Radical generation	C15. $CO + ^* \rightleftharpoons CO^*$
C2. $CH_4 + O^* \rightleftharpoons CH_3\bullet + OH^*$	C16. $C_2H_4 + O^* \rightleftharpoons C_2H_4O^*$
C3. $C_2H_6 + O^* \rightleftharpoons C_2H_5\bullet + OH^*$	C17. $C_2H_4O^* + O^* \rightleftharpoons C_2H_3O^* + OH^*$
Regeneration of active sites	C18. $C_2H_3O^* + O^* \rightleftharpoons CH_2O^* + HCO^*$
C4. $2OH^* \rightleftharpoons H_2O^* + O^*$	C19. $CH_3O\bullet + O^* \rightleftharpoons CH_2O + OH^*$
C5. $H_2O^* \rightleftharpoons H_2O + ^*$	C20. $CH_2O + O^* \rightleftharpoons CHO\bullet + OH^*$
Dehydrogenation to ethylene	C21. $CHO\bullet + O^* \rightleftharpoons CO + OH^*$
C6. $C_2H_5\bullet + O^* \rightleftharpoons C_2H_4 + OH^*$	**Coverage of active site**
Radical quenching	C22. $CO_2 + ^* \rightleftharpoons CO_2^*$
C7. $HO_2\bullet + O^* \rightleftharpoons O_2 + OH^*$	**Generation of HO_2 radical**
C8. $HO_2\bullet + ^* \rightleftharpoons OH\bullet + O^*$	C23. $H_2O_2 + O^* \rightleftharpoons HO_2\bullet + OH^*$
Non-selective oxidation	**Consumption of active O***
C9. $C_2H_4 + O^* \rightleftharpoons C_2H_3\bullet + OH^*$	C24. $H_2 + O^* \rightleftharpoons H\bullet + OH^*$
C10. $CH_3\bullet + O^* \rightleftharpoons CH_3O^*$	C25. $OH\bullet + O^* \rightleftharpoons O\bullet + OH^*$
C11. $CH_3O^* + O^* \rightleftharpoons CH_2O^* + OH^*$	C26. $H_2O + O^* \rightleftharpoons OH\bullet + OH^*$
C12. $CH_2O^* + O^* \rightleftharpoons CHO^* + OH^*$	

S2. Catalysts and *realistic* sets of catalyst descriptors

Table S2.1. OCM real catalysts used in the present work in order to identify realistic combinations of catalyst descriptors for the microkinetic simulations.

Dataset	Reference work	Catalysts
1	Kondratenko et al.[10]	La_2O_3, 0.1%Mn-9.1%Sr/La_2O_3, 0.1%Ba-9.1%Sr/La_2O_3, 0.1%Li-9.1%Sr/La_2O_3, 0.1%Na-9.1%Sr/La_2O_3, 0.1%Cs-9.1%Sr/La_2O_3, 0.1%Mn-1.0%Ba/La_2O_3, 0.1%Li-0.1%Ba/La_2O_3, 9.1%Na-0.1%Ba/La_2O_3, 0.1%Cs-0.1%Ba/La_2O_3, 0.1%Mn-9.1%Mg/La_2O_3, 8.3%Sr-8.3%Mg/La_2O_3, 0.9%Ba-9.0%Mg/La_2O_3, 0.1%Li-9.1%Mg/La_2O_3, 0.1%Na-9.1%Mg/La_2O_3, 0.9%Cs-9.0%Mg/La_2O_3, 8.3%Mn-8.3%Li/La_2O_3, 0.1%Mn-9.0%Na/La_2O_3, 8.3%Mn-8.3%Cs/La_2O_3, 8.3%Li-8.3%Na/La_2O_3, 0.1%Cs-9.1%Na/La_2O_3, 0.1%Li-9.1%Cs/La_2O_3, MgO, 8.3%Ba-8.3%Sr/MgO, 8.3%Na-8.3%Sr/MgO, 8.3%Cs-8.3%Sr/MgO, 0.1%Mn-9.1%Ba/MgO, 8.3%Cs-8.3%Ba/MgO, 0.1%Mn-9.1%La/MgO, 8.3%Sr-8.3%La/MgO, 0.9%Ba-9.0%La/MgO, 8.3%Li-8.3%La/MgO, 8.3%Na-8.3%La/MgO, 8.3%Cs-8.3%La/MgO, 0.1%Mn-9.1%Cs/MgO, 0.1%Na-9.1%Cs/MgO
2	Olivier et al.[11]	12.5%Sr/La_2O_3, 10%Sn-20%Li/MgO, 20%La/MgO, 10%La-20%Sr/CaO, 20%La/MgO, 10%La/CaO, 20%(Pt-V-Li)/MgO, 10%La/MgO
3	Kondratenko et al.[10]	10%Li/MgO, 20%Li/MgO, 30%Li/MgO
4	Olivier et al.[11]	9.1%Li-0.1%Ba/MgO, 9.1%Li-0.1%Na/MgO, 9.1%Li-0.1%Cs/MgO
5	Huang et al.[12]	3.6%Na-1.8%S-0.7%Zr-0.6%Mn/SiO_2, 4.3%Na1.1%S-0.1%W-0.3%P-0.7%Zr-0.6%Mn/SiO_2, 5.6%Na-1.9%S-0.3%W-0.5%P-1.6%Zr-0.3%Mn/SiO_2, 3.2%Na-0.4%S-0.3%W-0.8%Zr-0.6%Mn/SiO_2, 2.7%Na-1.0%S-0.2%W-0.1%P-1.1%Zr-0.42%Mn/SiO_2, 4.0%Na-0.9%S-0.2%W-0.1%P-1.0%Zr-0.4%Mn/SiO_2, 3.5%Na-1.8%S-0.7%Zr-0.5%Mn/SiO_2, 3.8%Na-1.4%S-0.3%W-0.1%P-2.0%Zr-0.6%Mn/SiO_2, 4.9%Na-1.3%S-0.2%W-0.9%P-0.7%Zr-0.4%Mn/SiO_2, 4.3%Na-0.7%S-0.3%W-0.4%P-0.8%Zr-0.5%Mn/SiO_2, 3.3%Na-0.1%S-0.3%W-0.5%P-1.1%Zr-0.6%Mn/SiO_2, 5.7%Na-0.3%S-0.1%W-0.5%P-0.8%Zr-0.6%Mn/SiO_2, 4.1%Na-1.0%S-0.3%W-0.6%P-1.7%Zr-0.6%Mn/SiO_2, 1.9%Na-0.7%S-0.1%W-0.1%P-0.6%Mn/SiO_2
6	Shahri et al.[13]	5%Na_2WO_4-2%Mn/SiO_2, 0.5%Ce-5%Na_2WO_4-2%Mn/SiO_2, 1.0%Ce-5%Na_2WO_4-2%Mn/SiO_2, 2.5%Ce-5%Na_2WO_4-2%Mn/SiO_2, 5.0%Ce-5%Na_2WO_4-2%Mn/SiO_2, 8.0%Ce-5%, Na_2WO_4-2%Mn/SiO_2, 1.0%Ce-5%Na_2WO_4-2%Mn/SiO_2

The results of a methodology previously proposed by our research group[2] to reproduce experimental performances via microkinetic simulations are shown in Figure S2.1 for the literature datasets herein considered. In this figure, the empty circles represent the *virtual* catalysts (i.e. combination of catalyst descriptors) which were identified as *realistic*, i.e. able to reproduce performances of real catalysts (full triangles) at a given set of operating conditions. The catalysts descriptors that were found to be discriminating between the several catalyst groups[2] are reported in Figure S2.2, together with their value ranges indicated via bar charts. The full scale corresponds to the descriptor ranges as originally identified from literature[2]. The coloured bars indicate the ranges for realistic descriptors after the applying the methodology to each dataset. It can be observed that the value ranges could be narrowed as to exclude non-realistic, often too optimistic performances[14].

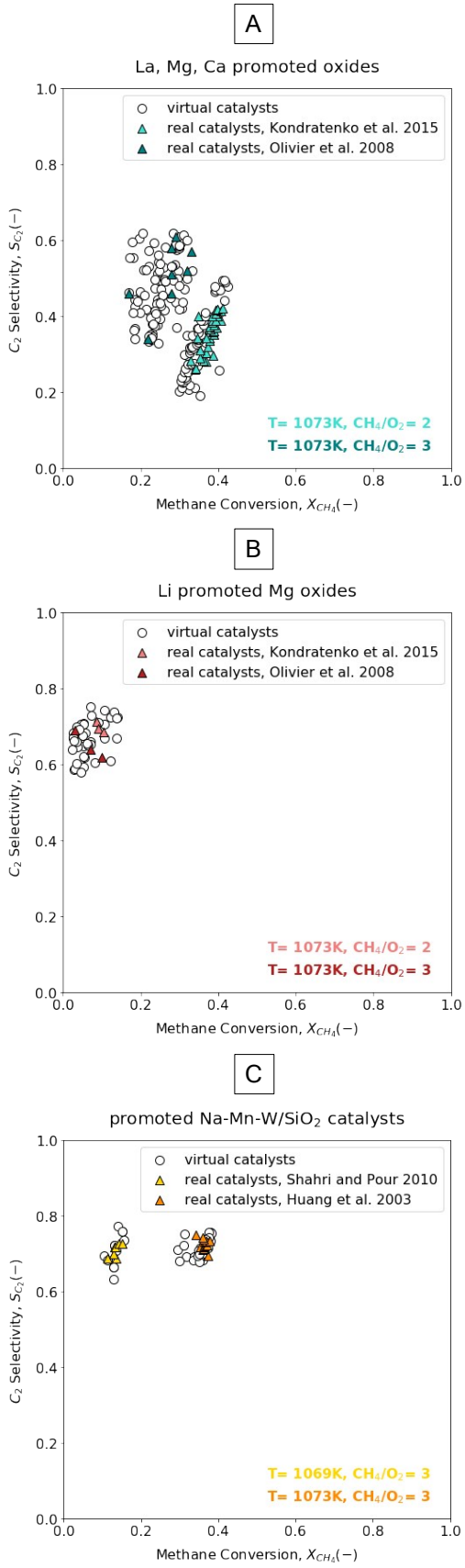

Figure S2.1. Output of the methodology described in our previous work[2], applied to the six datasets of interest in the present work to identify realistic catalyst descriptor combinations. The operating conditions for the simulations are the same as the ones reported in literature for the experimental datasets[10-13].

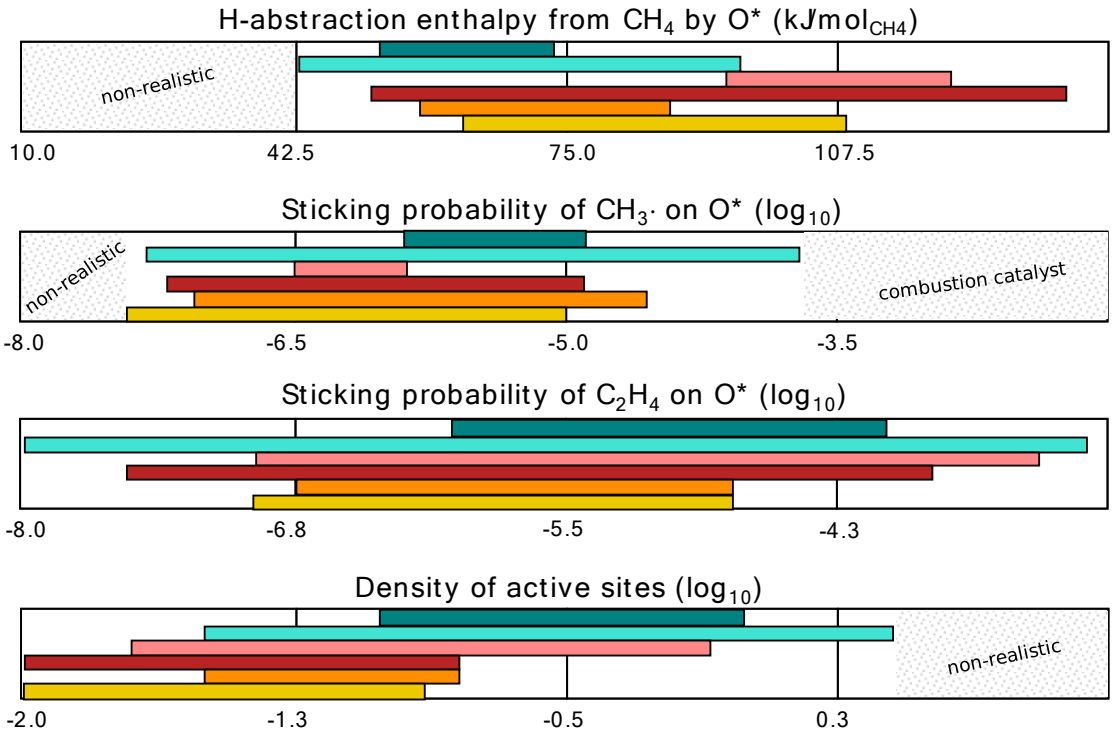

Figure S2.2. Most significant catalyst descriptors for the identification of the realistic OCM catalysts used in the present work. The color scheme refers to the different datasets from literature and it is the same as in Figure S2.1.

S3. Additional results about catalyst ranking in isothermal operation

Table S3.1. Correlation matrix for all the pairwise comparisons performed for isothermal scenarios in an operating range considered to be typical for isothermal OCM: T= 1023 – 1073 K, CH_4/O_2= 2-5.

			dataset *isoth2*							
	T(K)	→	1023				1073			
	↓	**CH_4/O_2**	2	3	4	5	2	3	4	5
dataset *isoth1*	1023	2	1	0.99	0.97	0.95	0.98	0.97	0.94	0.92
		3		1	0.99	0.98	0.98	0.98	0.97	0.96*
		4			1	1	0.96	0.98	0.98	0.97
		5				1	0.95	0.98**	0.99	0.98
	1073	2					1	0.99	0.97	0.95
		3						1	0.99	0.98
		4							1	0.99
		5								1

*case graphically reported in Figure 3/A

**case graphically reported in Figure S3.1/A

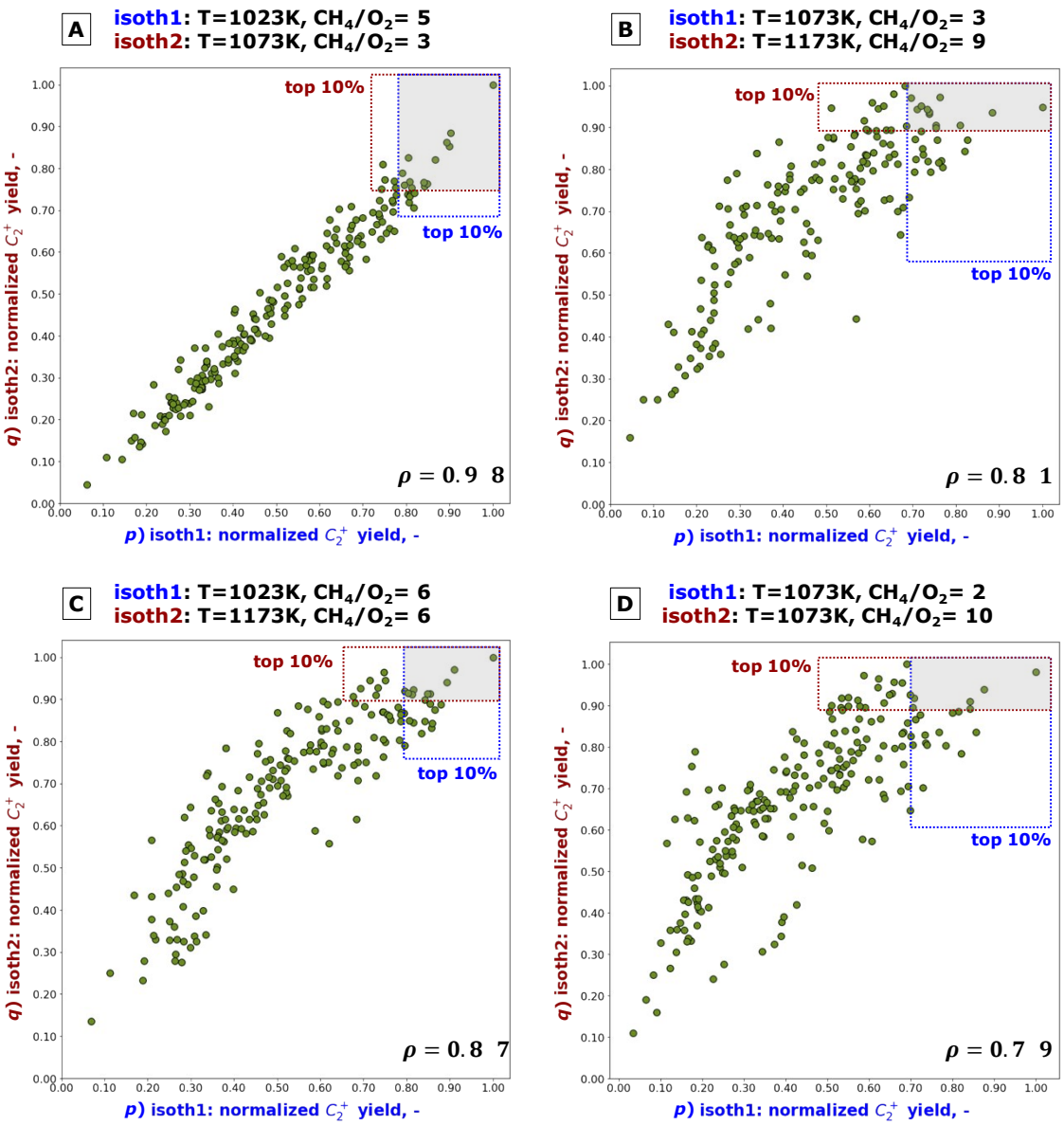

Figure S3.1. Pairwise comparisons of the performance ranking of the 220 realistic OCM catalysts, for four isothermal cases, with operating conditions as indicated in the top legends.

Table S3.2. Correlation matrixes for all the pairwise comparisons performed for isothermal scenarios by keeping CH_4/O_2 constant and varying the operating T.

			dataset *isoth2*			
	CH_4/O_2	→	2			
	↓	**T(K)**	1023	1073	1123	1173
dataset *isoth1*	2	1023	1	0.98	0.94	0.88
		1073		1	0.98	0.94
		1123			1	0.97
		1173				1
…						
			dataset *isoth2*			
	CH_4/O_2	→	6			
	↓	**T(K)**	1023	1073	1123	1173
dataset *isoth1*	6	1023	1	0.98	0.94	0.87**
		1073		1	0.97	0.94*
		1123			1	0.97
		1173				1
…						
			dataset *isoth2*			
	CH_4/O_2	→	10			
	↓	**T(K)**	1023	1073	1123	1173
dataset *isoth1*	10	1023	1	0.97	0.92	0.86
		1073		1	0.98	0.87
		1123			1	0.93
		1173				1

*case graphically reported in Figure 3/C

**case graphically reported in Figure S3.1/C

Table S3.3. Correlation matrixes for all the pairwise comparisons performed for isothermal scenarios by keeping the operating T constant and varying the inlet CH_4/O_2.

			dataset *isoth2*								
	T(K)	→	1023								
	↓	**CH_4/O_2**	2	3	4	5	6	7	8	9	10
dataset *isoth1*	1023	2	1	0.99	0.97	0.95	0.92	0.90	0.87	0.85	0.82
		3		1	0.99	0.98	0.97	0.95	0.93	0.91	0.89
		4			1	1	0.99	0.98	0.96	0.95	0.93
		5				1	1	0.99	0.98	0.97	0.95
		6					1	1	0.99	0.98	0.97
		7						1	1	0.99	0.98
		8							1	1	0.99
		9								1	1
		10									1
	T(K)	→	1073								
	↓	**CH_4/O_2**	2	3	4	5	6	7	8	9	10
dataset *isoth1*	1073	2	1	0.99	0.97	0.95	0.93	0.87	0.85	0.82	0.79**
		3		1	0.99	0.98	0.97	0.91	0.90	0.87	0.85
		4			1	0.99	0.98	0.94	0.93	0.91	0.89
		5				1	1	0.97	0.95	0.94	0.92
		6					1	0.98	0.97	0.96	0.95
		7						1	1	0.99	0.98
		8							1	1	0.99
		9								1	1
		10									1
	T(K)	→	1123								
	↓	**CH_4/O_2**	2	3	4	5	6	7	8	9	10
dataset *isoth1*	1123	2	1	0.99	0.95	0.94	0.91	0.84	0.81	0.78	0.76*
		3		1	0.99	0.98	0.96	0.88	0.86	0.83	0.80
		4			1	0.99	0.98	0.91	0.89	0.87	0.85
		5				1	0.99	0.94	0.92	0.90	0.89
		6					1	0.95	0.94	0.93	0.92
		7						1	1	0.99	0.98
		8							1	1	0.99
		9								1	1
		10									1
	T(K)	→	1173								
	↓	**CH_4/O_2**	2	3	4	5	6	7	8	9	10
dataset *isoth1*	1173	2	1	0.99	0.97	0.94	0.90	0.87	0.85	0.81	0.76
		3		1	0.99	0.98	0.95	0.93	0.91	0.88	0.84
		4			1	1	0.98	0.96	0.95	0.92	0.90
		5				1	1	0.98	0.97	0.95	0.93
		6					1	1	0.99	0.97	0.95
		7						1	0.99	0.97	0.96
		8							1	0.99	0.99
		9								1	1
		10									1

*case graphically reported in Figure 3/D

**case graphically reported in Figure S3.1/D

S4. Additional results about the feed composition effect in isothermal operation

Figure 3/D in the manuscript reports the comparison of the following isothermal scenarios: p) $T|_{isoth1}$= 1123 K, $CH_4/O_2|_{isoth1}$= 2 and q) $T|_{isoth2}$= 1123 K, $CH_4/O_2|_{isoth2}$= 10, in order to assess the effect of feed composition on the catalyst ranking. The descriptors which were found to be significantly different between the top 10% performing catalysts in these two scenarios are: the chemisorption enthalpy of oxygen, the density of active sites on the catalyst surface and the specific surface area. As shown in Figure S4.1, these three properties take on significantly lower values for the top-performing catalysts in scenario q, corresponding to oxygen-lean conditions. A p value < 0.01 in the Kruskal-Wallis test was considered as threshold for significance: the null hypothesis of equal mean ranks among the distributions of the descriptors in the two quadrants can be rejected.

For a given set of operating conditions, these three descriptors influence the concentration of oxygen species under the form of O* on the catalyst surface. As shown in Figure S4.2, a lower concentration of O* (mmolO*/kg_{CAT}) is obtained in case of lower density of active sites (mmol*/m^2, where * represents a surface vacancy), lower specific surface area (m^2/kg_{CAT}) and weaker oxygen chemisorption (lower enthalpy of reaction: $O_{2(g)} + 2* \rightarrow 2O*$). These properties correspond to catalyst cat 2 in the figure.

For a given catalyst, the actual concentration of O* depends not only on the intrinsic catalyst properties, i.e. the descriptors, but also on the operating conditions. For instance, for each catalyst, the surface O* concentration is higher in case of an oxygen-rich gas feed, because the chemisorption on the surface is favoured at higher partial pressure of oxygen in the gas.

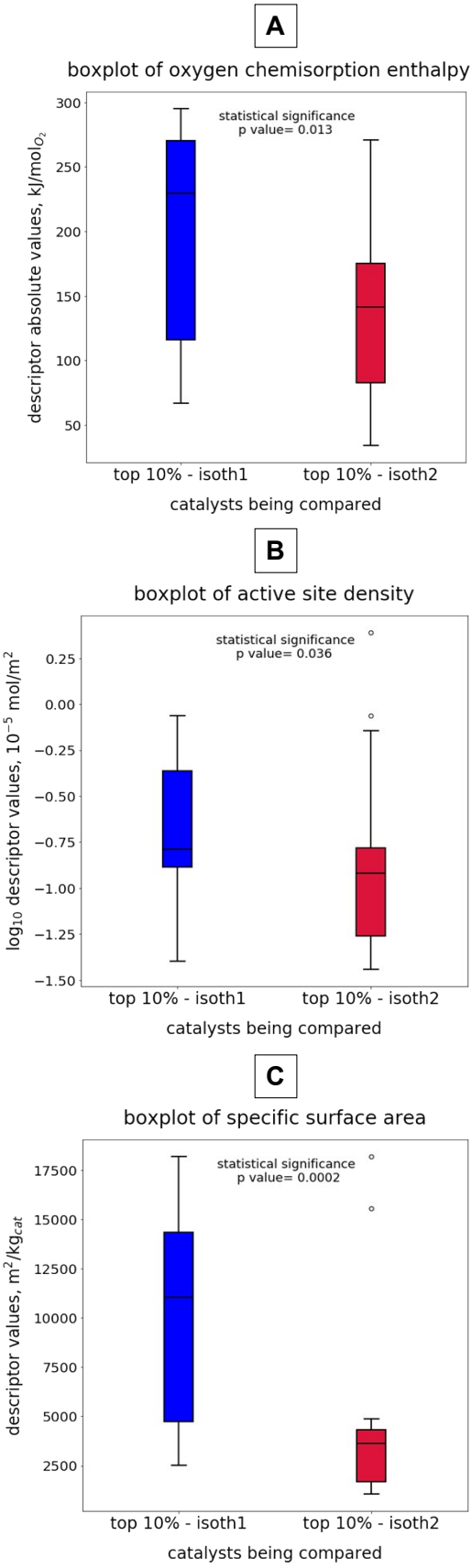

157

158 *Figure S4.1. Output of the statistical tests, referring to the top 10% catalysts in Figure 3/D: p) $T|_{isoth1}$= 1123 K,*
159 *$CH_4/O_2|_{isoth1}$= 2, q) $T|_{isoth2}$= 1123 K, $CH_4/O_2|_{isoth2}$= 10.*

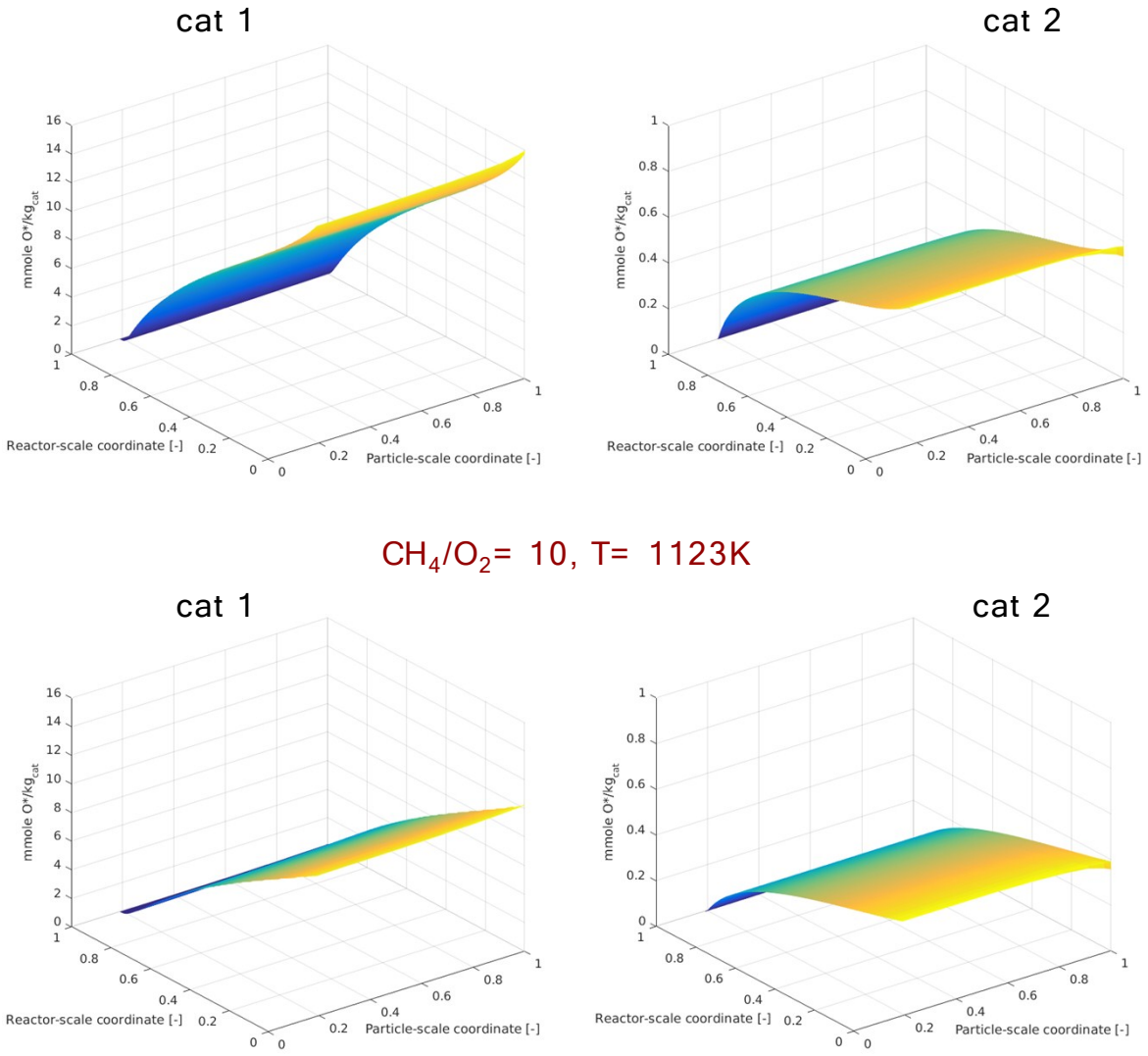

Figure S4.2. Concentration of O on the surface of two catalysts corresponding to the simulations reported in Table S4.1. The two catalysts differ in terms of oxygen chemisorption enthalpy (cat 1= 100 kJ/mol, cat 2= 60 kJ/mol), active site density (cat 1= $9.3 \cdot 10^{-6}$ mol/m^2, cat 2= $1.3 \cdot 10^{-6}$ mol/m^2) and specific surface area (cat 1= 5600 m^2/kg$_{cat}$, cat 2= 2800 m^2/kg$_{cat}$). These two catalysts are representative of the groups top 10% isoth1 and top 10% isoth2 from Figure S4.1.*

In Table S4.1 the performances of the two catalysts in Figure S4.2 are reported in the two scenarios from Figure 3/D. As described above, the average concentration of surface oxygen is higher in case of an oxygen-rich feed (CH_4/O_2= 2) for both catalysts. The increase in surface oxygen at low CH_4/O_2 is more pronounced for the cat 2, which is characterized by lower concentration of free sites * and weaker chemisorption (+32% surface O* for cat 1 vs 45% cat 2). However, the most important observation is that cat 1, characterized by a more than 20-times higher concentration of surface oxygen at both methane-to-oxygen ratios, performs

significantly better than cat 2 in case of an oxygen-rich feed (CH_4/O_2= 2). However, when the gas phase is oxygen-starved (CH_4/O_2= 10), a lower concentration of surface oxygen (cat 2) is more beneficial in terms of C_{2+} yield, thus resulting in reserved ranking of the two catalysts.

Table S4.1. Performances of the two catalysts reported in Figure S.4.2 for isothermal operation at two extreme methane-to-oxygen ratios. In bold the confirmation that a higher concentration of surface oxygen vacancies is beneficial in the oxygen-rich scenario, while being detrimental in the oxygen-lean case.

T= 1123K	**A. CH_4/O_2= 2**		**B. CH_4/O_2= 10**	
	cat 1	cat 2	cat 1	cat 2
Average O* (mmol/kg_{cat})	7.30	0.32	5.49	0.22
GHSV (h^{-1})	126371	29764	299606	66529
X_{O2}	100%	100%	100%	100%
X_{CH4}	39.2%	38.5%	14.2%	14.5%
S_{C2+}	46.5%	44.0%	78.5%	78.8%
Y_{C2+}	**18.2%**	16.9%	**11.1%**	11.4%

$$R_{selec} = \frac{m\ o_{CH_3}\ l}{s^t \times m^3} c\ o\ n\ v\ e\ t\ o\ C_2H_6, C_3H_7, C_3H_8$$

$$R_{unsele} = \frac{m\ o_{CH_3}\ l}{s^c \times m^3} c\ o\ n\ v\ e\ t\ o\ CH_2O, CH_3O\cdot, CH_3O*$$

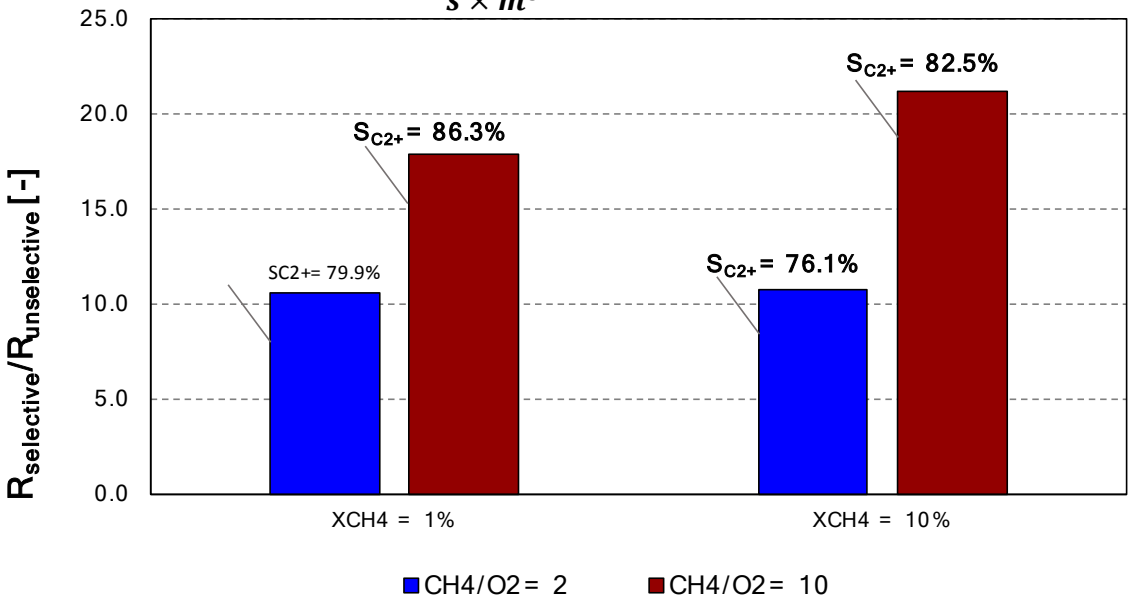

Figure S4.3. Comparison of selective vs non-selective conversion rates of methyl radicals at two methane conversion levels for cat 1 in Figure S4.2. $R_{selective}$ is calculated via the rates of reactions G9, G10 and G11 reported in Table S1.1; $R_{unselective}$ is calculated via the rates of reactions G6, G7, G8 and C10 reported in Tables S1.1 and S1.2.

S5. Results about catalyst ranking in adiabatic operation

The pairwise comparisons of three adiabatic scenarios is shown in Figure S5.1. For some catalysts, indicated by empty circles in the figure, complete oxygen conversion could not be achieved even at the minimum GHSV constraint in the lower inlet temperature scenario considered in each comparison. This results in a low C_{2+} yield and, consequently, a low ranking for this scenario. Most of these catalysts achieve high/complete oxygen conversion in the higher inlet temperature scenario, hence, their ranking results significantly higher. The number of catalysts for which complete oxygen conversion cannot be achieved is obviously more pronounced for the lowest inlet temperature (i.e. 800 K), thus explaining the higher amount of empty circles in Figure S5.1/B compared to Figure S5.1/C. This implies that for these catalysts, the light-off temperature[6] is in between the inlet temperature of both scenarios considered (i.e. between 800 K and 853 K in Figure S5.1/A and between 853 K and 900 K in Figure S5.1/C). These catalysts were excluded from the analysis of the correlation coefficient because the pairwise ranking comparisons should be performed at comparable oxygen conversion level.

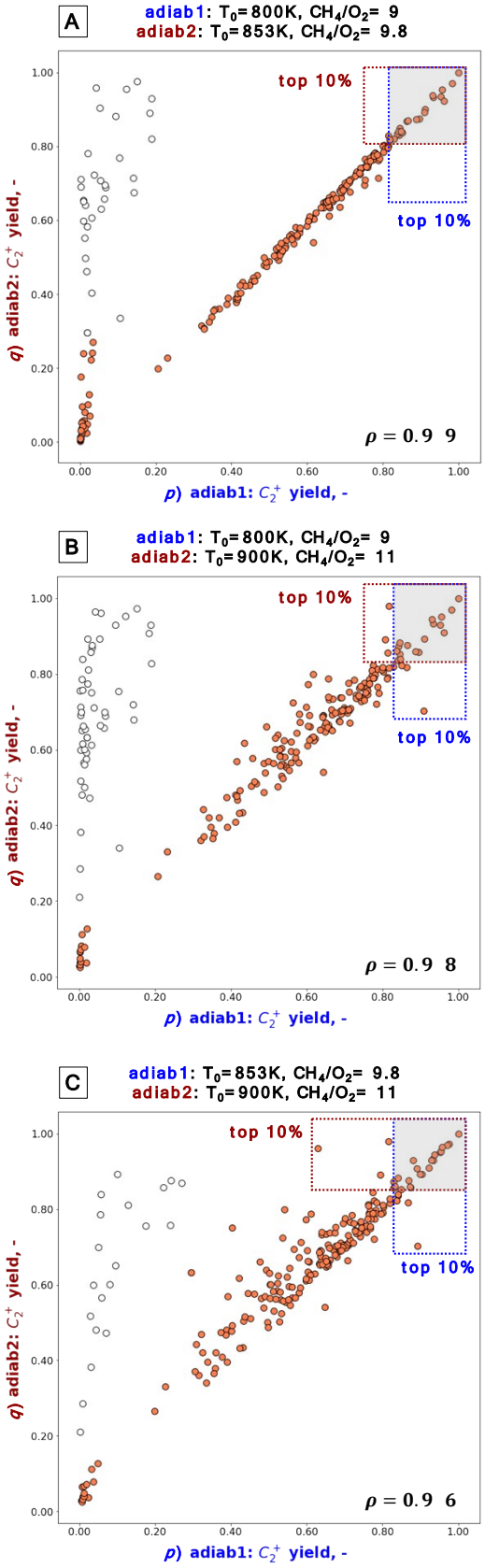

Figure S5.1. Pairwise comparisons of the performance ranking of the 220 realistic OCM catalysts, for three adiabatic scenarios, with operating conditions as indicated in the top legends. Empty circles correspond to catalysts for which light-off (X_{O2}≥ 50%) was achieved only in scenario q) and not in scenario p), and for this reason are excluded from the analysis of the correlation coefficient.

S6. Additional results about catalyst ranking in isothermal vs adiabatic operation

Table S6.1. Correlation matrixes for all the pairwise comparisons performed for isothermal vs adiabatic operation.

			dataset *isoth*								
dataset *adiab*	**T, T_0 (K)**	→	1023								
	↓	**CH_4 /O_2**	2	3	4	5	6	7	8	9	10
	800	9.0	0.47	0.51	0.55	0.57	0.59	0.61	0.62	0.63	0.64***
	853	9.8	0.48	0.52	0.56	0.60	0.61	0.62	0.63	0.64	0.65
	900	11.0	0.51**	0.57	0.61	0.63	0.64	0.66	0.68	0.69	0.71
	T, T_0 (K)	→	1073								
	↓	**CH_4 /O_2**	2	3	4	5	6	7	8	9	10
	800	9.0	0.52	0.58	0.59	0.61	0.62	0.63	0.65	0.66	0.68
	853	9.8	0.52	0.58	0.59	0.62	0.63	0.64	0.65	0.67	0.68
	900	11.0	0.57	0.64	0.65	0.67	0.70	0.72	0.74	0.76	0.77
	T, T_0 (K)	→	1123								
	↓	**CH_4 /O_2**	2	3	4	5	6	7	8	9	10
	800	9.0	0.56	0.64	0.67	0.68	0.71	0.72	0.74	0.74	0.76
	853	9.8	0.56	0.64	0.67	0.68	0.71	0.72	0.74	0.75	0.76
	900	11.0	0.59	0.70	0.72	0.75	0.76	0.78	0.80	0.83	0.85
	T, T_0 (K)	→	1173								
	↓	**CH_4 /O_2**	2	3	4	5	6	7	8	9	10
	800	9.0	0.57	0.65	0.68	0.70	0.73	0.77	0.79	0.82	0.83
	853	9.8	0.57	0.65	0.68	0.70	0.74	0.77	0.80	0.82	0.83
	900	11.0	0.57****	0.70	0.73	0.77	0.79	0.83	0.84	0.86	0.86*

*case graphically reported in Figure 4/A
**case graphically reported in Figure 4/B
***case graphically reported in Figure 4/C
**** case graphically reported in Figure 4/D

S7. Additional results about the comparison of 1st quadrant and 2nd quadrant catalysts

The most significant difference between the catalysts in the two quadrants is related to the sticking probability of ethylene on surface oxygen, which is the most influential descriptor for C_2H_4 oxidation on the catalyst surface, i.e. reaction [4] in Table 2. A p value < 0.01 in the Kruskal-Wallis test was considered as threshold for significance: the null hypothesis of equal mean ranks among the distributions of the descriptors in the two quadrants can be rejected.

In terms of catalytic properties, this descriptor is representative of the nature of the oxygen species on the catalyst surface[2] and can be related to the catalyst basicity[15] and electronic properties[16]. This observation points again to the role of surface oxygen as key discriminating factor in the ranking of catalysts as a function of the operating conditions and operating mode.

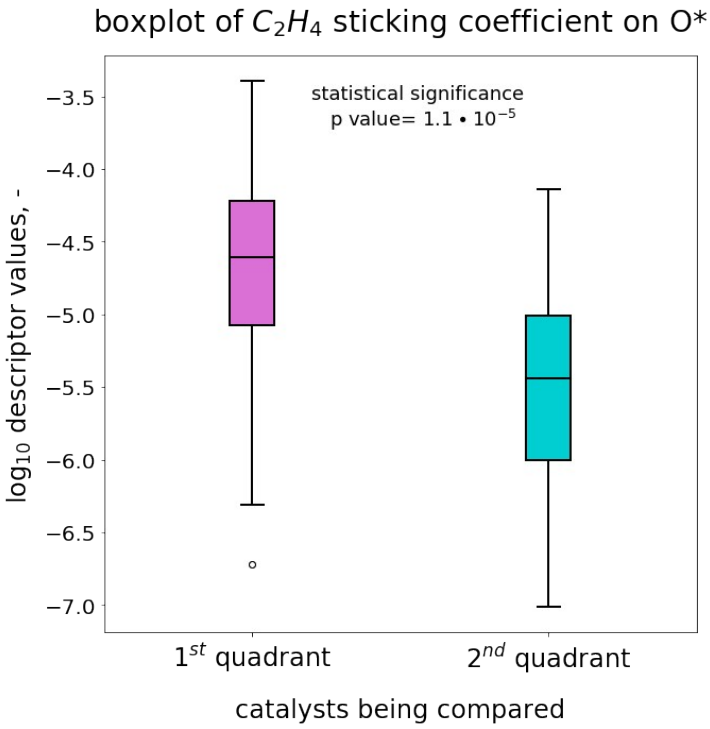

Figure S7.1. Referring to Figure 5/A: isoth) T= 1023K, CH_4/O_2= 2, adiab) T_0= 900K, CH_4/O_2= 11.

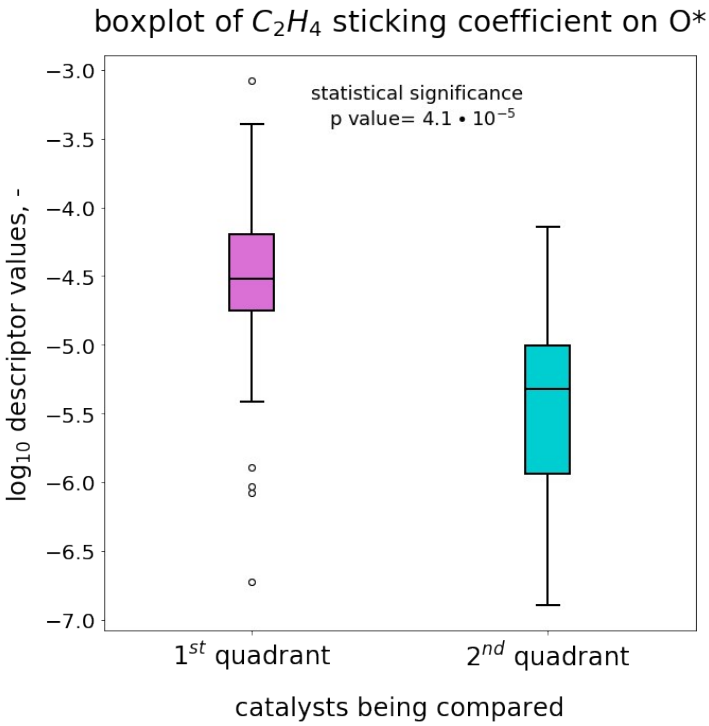

235

236 *Figure S7.2. Referring to Figure 5/B: isoth) T= 1173 K, CH_4/O_2= 2, adiab) T_0= 900 K, CH_4/O_2= 11.*

237

238 The predominance of ethylene consecutive oxidation for the 1st quadrant catalysts, identified
239 and described via Delplots in section 4.2 of the manuscript, is visualized in a simplified reaction
240 pathway analysis in Figure S7.3.

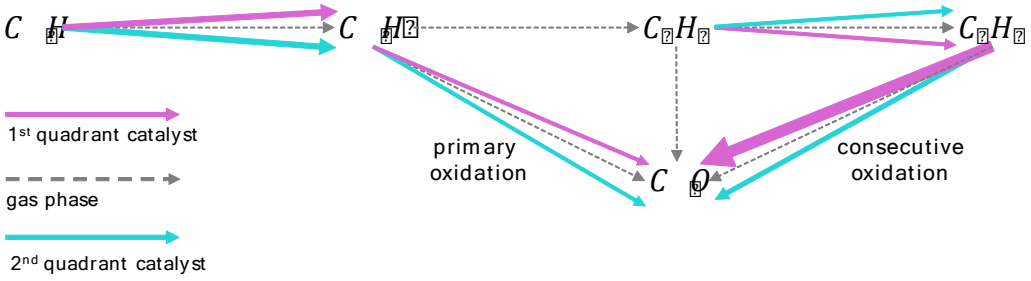

241
242 *Figure S7.3. Qualitative reaction path for the oxidation routes associated with Delplots of the two catalysts in*
243 *Figure 8 and S7.4, with thicker arrows referring to faster reactions.*

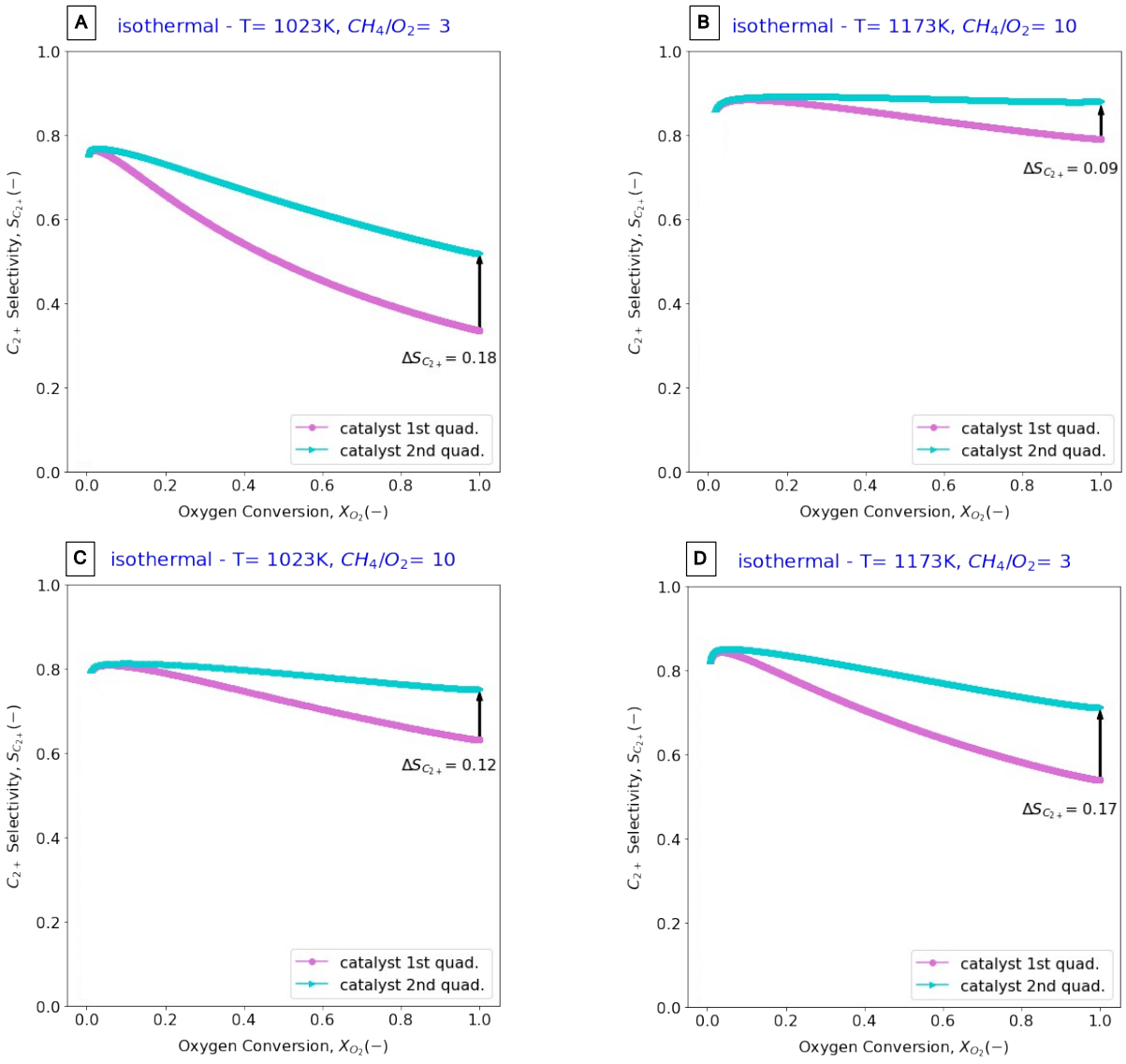

Figure S7.4. First-rank Delplots, i.e. selectivity vs conversion plots, for two catalysts belonging to the 1st (pink) and 2nd (light-blue) quadrants of Figure 5, for four isothermal (A, B, C, D), with operating conditions as indicated in the top legends. Figures S7.4/A and S7.4/B correspond to Figure 8/A and 8/B and are herein reported again for the sake of completeness.

The effect of operating temperature on the oxidation routes can be analysed by comparing the Delplots in Figure S7.4/A (1023 K) and Figure S7.4/D (1173 K). The reduction in primary and consecutive oxidation[17] can be observed, respectively, by the higher selectivity at differential conversion for both catalysts in Figure S7.4/D compared to Figure S7.4/A, and the less steep selectivity vs conversion evolution. However, despite the relevance of operating temperature for OCM kinetics, the relative isothermal performances of the two catalysts at higher temperature (1173 K - Figure/D) are very similar to the ones at 1023 K (Figure/A), with the

256 catalyst from the 2nd quadrant clearly outperforming the one from the 1st quadrant, especially at
257 high conversion. This confirms that temperature alone does not significantly impact the catalyst
258 ranking.
259 The effect of CH_4/O_2 can be observed by comparing Figure S7.4/C with Figure S7.4/A, and, in
260 particular in combination with higher temperature, with Figure S7.4/B. The reduced slope of
261 the selectivity evolution with conversion observed for both catalysts in Figure S7.4/C and
262 Figure S7.4/B points to the limitation of the consecutive oxidation of the products in an oxygen-
263 lean environment (high CH_4/O_2) thanks to the reduced availability of the oxidant.

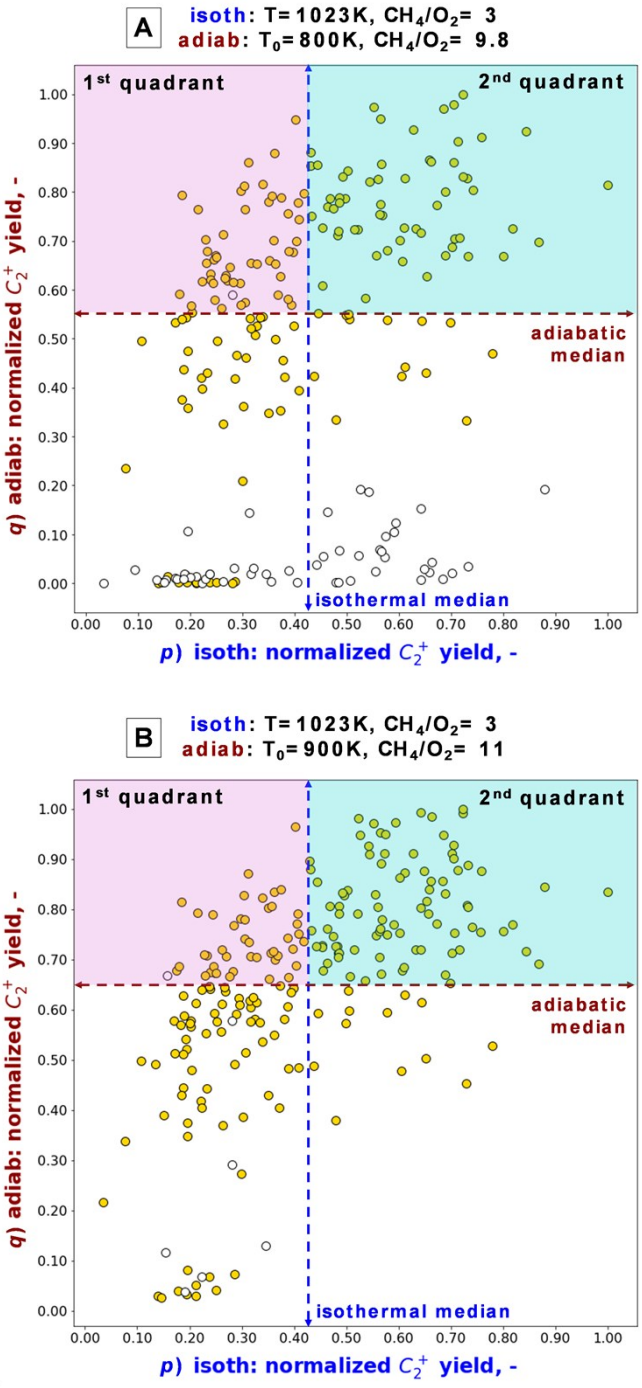

Figure S7.5. Comparison of the performance ranking of the 220 realistic OCM catalysts, for one isothermal scenario with two adiabatic scenarios, with operating conditions as indicated in the top legend. The dashed lines indicate the median rankings for both scenarios.

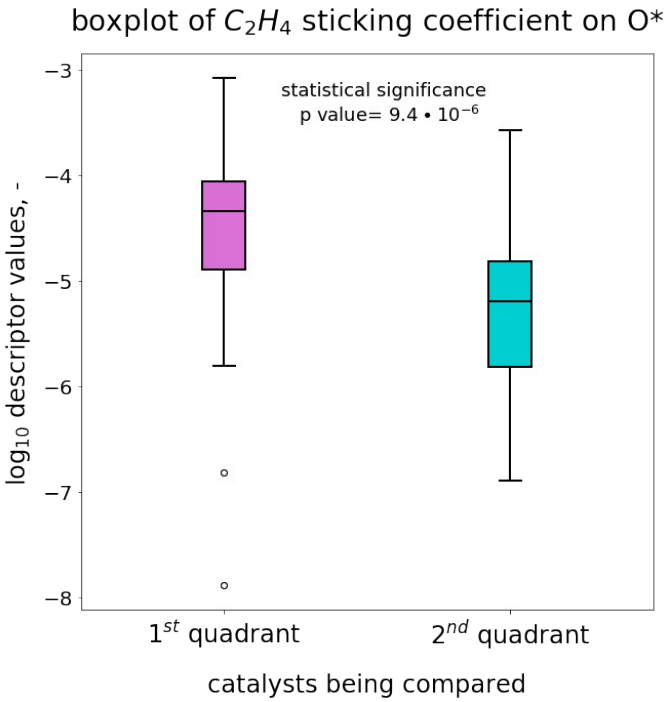

Figure S7.6. Referring to Figure S7.5/A: isoth) T= 1023 K, CH_4/O_2= 3, adiab) T_0= 800 K, CH_4/O_2= 9.8.

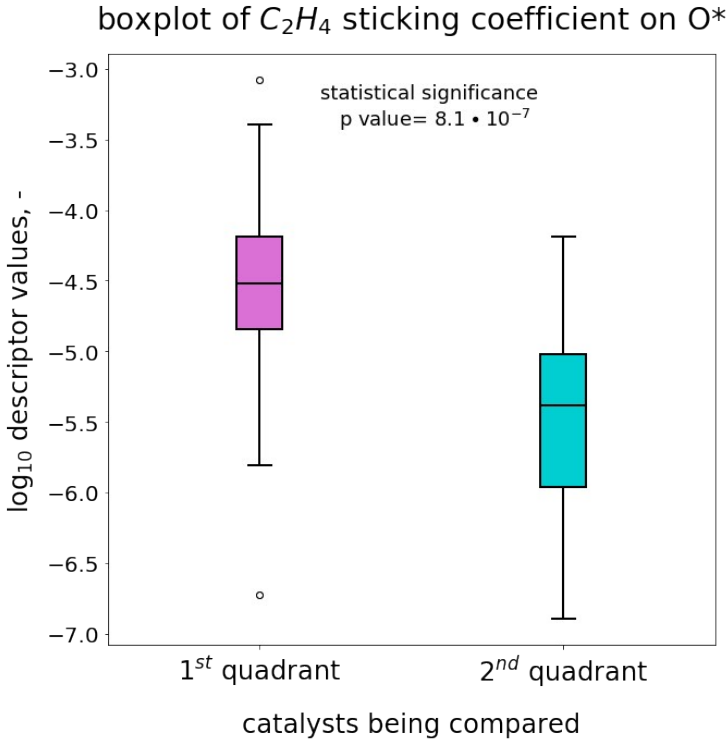

Figure S7.7. Referring to Figure S5.4/B: isoth) T= 1023K, CH_4/O_2= 3, adiab) T_0= 900K, CH_4/O_2= 11.

References

1. P. N. Kechagiopoulos, J. W. Thybaut and G. B. Marin, *Ind. Eng. Chem. Res.*, 2014, **53**, 1825-1840.
2. L. Pirro, P. S. F. Mendes, S. Paret, B. D. Vandegehuchte, G. B. Marin and J. W. Thybaut, *Catal. Sci. Technol.*, 2019, **9**, 3109-3125.
3. V. I. Alexiadis, J. W. Thybaut, P. N. Kechagiopoulos, M. Chaar, A. C. van Veen, M. Muhler and G. B. Marin, *Appl. Catal. B-Environ.*, 2014, **150**, 496-505.
4. V. I. Alexiadis, M. Chaar, A. C. van Veen, M. Muhler, J. W. Thybaut and G. B. Marin, *Appl. Catal. B-Environ.*, 2016, **199**, 252-259.
5. C. Karakaya, H. Zhu, C. Loebick, J. G. Weissman and R. J. Kee, *Catal. Today*, 2018, **312**, 10-22.
6. L. Pirro, A. Obradović, B. D. Vandegehuchte, G. B. Marin and J. W. Thybaut, *Ind. Eng. Chem. Res.*, 2018, **57**, 16295-16307.
7. J. J. Carberry and M. M. Wendel, *AIChE J.*, 1963, **9**, 129-133.
8. P. M. Couwenberg, Q. Chen and G. B. Marin, *Ind. Eng. Chem. Res.*, 1996, **35**, 415-421.
9. Q. Chen, P. M. Couwenberg and G. B. Marin, *Catal. Today*, 1994, **21**, 309-319.
10. E. V. Kondratenko, M. Schluter, M. Baerns, D. Linke and M. Holena, *Catal. Sci. Technol.*, 2015, **5**, 1668-1677.
11. L. Olivier, S. Haag, H. Pennemann, C. Hofmann, C. Mirodatos and A. C. van Veen, *Catal. Today*, 2008, **137**, 80-89.
12. K. Huang, X. L. Zhan, F. Q. Chen and D. W. Lu, *Chem. Eng. Sci.*, 2003, **58**, 81-87.
13. S. M. K. Shahri and A. N. Pour, *J. Nat. Gas Chem.*, 2010, **19**, 47-53.
14. A. Zunger, *Nature*, 2019, **566**, 447-449.
15. H. Borchert and M. Baerns, *J. Catal.*, 1997, **168**, 315-320.
16. Z. Zhang, X. E. Verykios and M. Baerns, *Catal. Rev.*, 1994, **36**, 507-556.

17. M. Y. Sinev, Z. T. Fattakhova, V. I. Lomonosov and Y. A. Gordienko, *J. Nat. Gas Chem.*, 2009, **18**, 273-287.